Solar Powered Unmanned Aerial Vehicle: A numerical approach in improving solar cell performance

Rowayne E. Murzello

School of Engineering and Physical Sciences,
Heriot-Watt University,
Edinburgh, EH14 4AS, United Kingdom
E-mail: rowayne.murzello@outlook.com

Mehdi Nazarinia*

School of Engineering and Physical Sciences,
Heriot-Watt University,
Edinburgh, EH14 4AS, United Kingdom
E-mail: m.nazarinia@hw.ac.uk
*Corresponding author

Amanda J. Hughes

School of Engineering,
University of Liverpool,
Liverpool, L69 3GH, United Kingdom
and
School of Engineering and Physical Sciences,
Heriot-Watt University,
Edinburgh, EH14 4AS, United Kingdom
E-mail: Amanda.Hughes2@liverpool.ac.uk

Abstract: Solar Powered Unmanned Aerial Vehicles (SPUAV) have numerous applications and can be considered as environmentally friendly vehicles since they use only the sun's energy for propulsion. It is known that the efficiency of solar cells decreases with temperature, therefore there are negative performance implications in hotter climates and it is important to have proper thermal management in place in order to ensure optimal solar cell performance. Therefore, a conceptional design was proposed which integrates a cooling duct inside the airfoil to provide convective cooling for the backside of solar cells. A MATLAB® program was first developed to model, size and provide optimum duct dimensions. Computational Fluid Dynamics (CFD) was also used to investigate the lift and drag characteristics of the modified airfoil. Heat transfer analysis on the solar array using CFD was performed to obtain solar cell temperatures of the baseline and modified design. The study investigated the lift and drag coefficients at different Reynolds numbers, angles of attack at cruising conditions and solar cell temperatures at different altitudes. A duct height of 2 mm and Reynolds number of 206,000 at an altitude of 1 km from sea level were the parameters and cruising conditions selected for testing the airfoils. Results obtained from the cruising

conditions showed that the maximum temperature drop was 3 °C and the cooling duct increased the lift force by 9 % per meter with an increase in drag of 13 %.

Keywords: cooling duct; Computational Fluid Dynamics; Unmanned Aerial Vehicle; solar powered UAV; heat transfer enhancement; solar cell.

Reference to this paper should be made as follows: Murzello, R.E., Nazarinia, M. and Hughes, A.J. (2019) 'Solar Powered Unmanned Aerial Vehicle: A numerical approach in improving solar cell performance', *International Journal of Aerodynamics*, Vol. x, No. x, pp.xxx–xxx.

Biographical notes: Mr Rowayne E. Murzello received his Bachelors in Mechanical Engineering from Heriot-Watt University in 2016. He is currently pursuing Masters of Applied Sciences in Mechanical Engineering from QueenâŁ™s University. His research interests are in computational fluid dynamics and renewable energy.

Dr Mehdi Nazarinia received his PhD in 2010 in Mechanical Engineering, Fluid Mechanics, at Monash University, Melbourne, Australia. He has worked as Wind Tunnel Support Engineer at Monash Wind Tunnel and Postdoctoral Fellow at the University of Melbourne since then. He is an Associate Director of Learning and Teaching and Associate Professor in Mechanical Engineering at the Heriot-Watt University, School of Engineering and Physical Sciences. His research interests are related to heavy vehicle aerodynamics, aircraft aerodynamics and solar and wind energy systems. He has published research papers at national and international journals, conference proceedings as well as chapters of books.

Dr Amanda J. Hughes received her PhD in mechanical engineering from Heriot-Watt University in 2015, where she studied hybrid photovoltaic and solar thermal collectors. She currently works as a lecturer at the University of Liverpool, were she is continuing her research into solar energy and heat transfer.

1 Introduction

Solar cells operate by converting solar energy from the sun into electrical energy which can be used for numerous applications. One major application is transportation, including research and development into Solar Powered Unmanned Aerial Vehicles (SPUAV) which utilise solar cells to provide electrical energy for powering electric motors. An advantage of using this fuel source is that compared to conventional jet propulsion engines, solar energy is free and can provide continuous flight. During the day, excess energy generated can be stored in batteries which will provide electricity when there is no sunlight and permits flight during the night. The ability to sustain flight for extended periods of time without refuelling allows SPUAV's to serve as an excellent surveillance vehicle for both civilian and military purposes with minimum impact on the environment.

The performance of SPUAV depends on various factors such as lift and drag, vehicle weight, and solar power management. One of the limitations of using solar cells is the operational efficiency which lies between 9 to 22% for polycrystalline and monocrystalline solar cells [1]. As a result, the wingspan of these aircraft has a larger aspect ratio in order to generate more energy to meet the payload requirements and increase flight endurance. It is known that the operational efficiency of solar cells is greatly reduced by temperature,

especially in hotter and harsher climates such as the United Arab Emirates (UAE) where average sea level inland temperatures during summer is 33°C [2]. During the summer season, during the month of July, the global solar radiation in the UAE peaks at 950 W/m^2 as measured in [3]. Solar cells have emissivity levels close to black bodies due to their dark colour and therefore absorb the majority of incident radiation, which gets trapped in the substrate. Encapsulation methods are used to increase solar cell durability by preventing UV ageing and weathering. As a result, the encapsulation increases the heat retention in the solar cell module due to low thermal conductivities. Therefore, thermal management techniques should be incorporated to improve overall system efficiency and ensure optimal performance.

The two main types of cooling mechanisms are active and passive systems. Active cooling systems employ water cooling or forced air cooling at the expense of increased energy usage and costs. Passive cooling systems rely on natural ventilation or convection of air which provides a substantial amount of cooling with almost zero or no energy consumption. McColl et al. [4] evaluated the annual performance of a 140 W photovoltaic module in Abu Dhabi which utilised active cooling with water and passive cooling with air for increased power generation. They showed that the water cooled PV module achieved a power output of 1 kWh/day compared to a passive cooling system which reached a maximum of 0.75 kWh/day during the summer season. The drawback with an active cooling system for a SPUAV is the increased weight and power consumption. Hence, the best method to reduce the operating temperature of solar cells for this application is to utilise a passive cooling system since power generation is vital for a SPUAV. The proposed design consists of a duct and heat sinks integrated into the wing of the SPUAV. The present study only considers passive cooling along the airfoil, since the wings of the SPUAV cover a large area exposed to sun where the cells are attached. A schematic of the proposed system is shown in Fig. 1. This system helps to provide convective cooling for the backside of solar cells through the duct utilizing a pressure difference between the inlet and outlet of the duct to create an airflow. Placing a heatsink, as shown in Fig. 1, underneath the solar cell within the wing geometry would maximise heat transfer and improve overall efficiency of the system. The addition of a channel underneath the upper surface of the wing can affect aerodynamic performance and increase drag force of the vehicle. The challenge is to provide useful passive cooling of the cells whilst keeping the overall drag force of the SPUAV as low as possible. Colozza and Dolce [5] showed that the solar cell temperature can be significantly reduced by a stream of air flowing in a duct located underside the solar cell array hence improving cell efficiency with minimum drag.

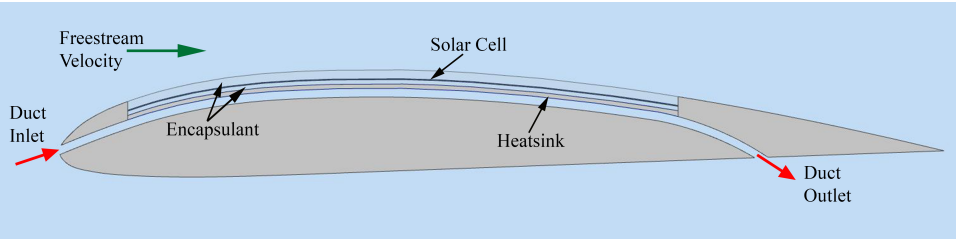

Figure 1: Schematic of the proposed passive design system comprised of Clark Y Airfoil section modified to incorporate the Cooling Duct

To the best knowledge of authors, there is limited research available in literature about cooling duct designs for solar aircraft or even solar powered vehicles which makes this conceptual idea important to investigate. The preliminary findings and results were presented initially in [6]. The present study improves on the preliminary results and considers a remote-controlled aircraft that has a Clark Y airfoil and monocrystalline solar cells with 22% cell efficiency. A maximum altitude of 2 km has been selected for this study due to the transmitter range. MATLAB® was used to develop a model, where all flight parameters are considered, to determine the optimum duct height based on the power gained by cooling and change in aerodynamic drag. Computational Fluid Dynamics (CFD) with ANSYS Fluent v14.5 was also used to obtain the lift and drag coefficients as well as performing heat transfer analysis to determine the solar cell temperature and pressure distribution around the wing and within the duct.

2 Methodology

The conceptual design for the cooling duct comprised of two main parts: analytical and computational approaches. Surveillance mission is selected for the UAV, hence a cruise altitude and speed of 1 km and 15 m/s are assumed, respectively. A Clark Y airfoil was selected as the base wing profile due to its improved lift to drag ratio which makes it suitable for aircraft with high aspect ratios [7].

The material properties used in the analysis are listed in Table 1. This includes Ethylene-Vinyl Acetate (EVA) which was used for encapsulation of C60 Solar Cell Mono Crystalline Silicon [8], with an efficiency of 22% and power coefficient of -0.4% per °C over 25°C. An aluminium plate was used as a heat sink for the modified airfoil and is part of the design of the cooling duct as shown in Fig. 1. This enhances heat transfer from the backside of the solar cells.

Table 1 List of material properties used in this article similar to [9].

Layer	Thickness (mm)	Thermal Conductivity (W/m K)	Density (kg/m^3)	Specific Heat Capacity (J/kg K)
Solar Cell	0.2	148	2330	677
EVA Encapsulant	0.5	0.35	960	2090
Aluminum Plate	1	202	2719	871
ABS Plastic	Null	1260	1080	1260

2.1 Analytical Calculations

Usually, SPUAV's fly up to an altitude of 2 km and therefore the atmospheric properties vary significantly from the launch altitude. Standard atmospheric equations (see for example [10]) and ideal gas equations of state were used to obtain the air temperature, pressure and density at various altitudes. Standard atmospheric relations were used to calculate atmospheric parameters [11]. The lapse rate was $L_r = 0.0065$ K/m since all calculations

were done for the Earth's troposphere layer. Equations 1 and 2 were used to calculate the air temperature (K) and pressure (Pa), respectively.

$$T_A = T_0 - (L_r Z) \tag{1}$$

$$p_A = p_0 \left(\frac{T_A}{T_0} \right)^{\frac{g}{L_r R}} \tag{2}$$

where subscript 0 is related to the standard values at the sea level, g is gravitational acceleration, R is specific gas constant of air (J/kg K) and Z is the altitude above sea level (m). Sutherland's law was used to calculate the dynamic viscosity of air within the troposphere layer where the reference temperature was considered as $T_s = 110$ K [12].

2.1.1 PV Cooling

For a solar aircraft with PV cells installed on the wings, if the lower surface is considered as an insulated surface and radiation is negligible, the heat loss will be by convection and conduction through the top [13, 14]. Fig. 2 shows a schematic of heat transfer mechanisms from the PV cell through the surface and ducts. The Reynolds number is calculated with the airfoil chord as a characteristic length. The Nusselt numbers, convective heat transfer coefficient on the wing surface, conductive thermal resistance were all calculated from the established empirical relationships available in the literature such as [13] and [15]. The total solar energy incident on an area of solar cell, Q_I, is calculated using Eq. 3:

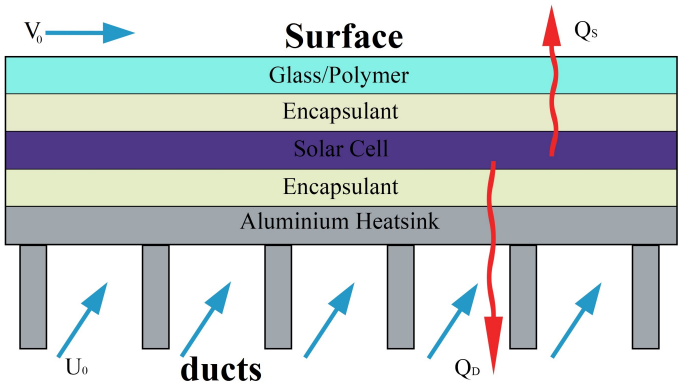

Figure 2: Schematic of heat transfer mechanisms from PV solar cell through surface and ducts. The air flow over the surface and in the ducts are into the page. V_0 is the aircraft velocity, Q_s is the surface heat loss from PV cell (W/m^2) and Q_D is the duct heat loss (W/m^2).

$$Q_I = I_r A_{PV} \tag{3}$$

where I_r is the solar radiation (W/m^2) and A_{PV} is solar cell area (m^2). The power output from the solar cells was calculated using the PV efficiency and its area as shown in Eq. 4:

$$Q_{PV} = \eta_{PV} I_r A_{PV} \tag{4}$$

where η_{PV} is the solar cell efficiency provided by the manufacturer.

Subtracting the total solar power from the generated electrical power yields the waste heat as shown in Eq. 5,

$$Q_H = Q_I - Q_{PV} \tag{5}$$

where Q_H is the heat loss from the PV cell (W/m^2).

The heat loss from the PV cell can also be found considering all of the waste heat is removed as seen in Eq. 6,

$$Q_s = U_s \left(T_{PV} - T_A\right) \tag{6}$$

where Q_s is the surface heat loss from PV cell (W/m^2), U_s is the surface cooling thermal resistance (W/m^{2}K) and T_{PV} (K) can be calculated using Eq. 7:

$$T_{PV} = \frac{Q_s + (T_A U_s)}{U_s}. \tag{7}$$

The cooling duct concept would utilise an air duct as shown in Fig. 2, where the air flow over the surface and in the ducts are into the page. This schematic shows heat loss through the top surface and the ducts where there is an additional method of convective heat transfer. It should be mentioned that radiative heat transfer was neglected following the discussions in [13].

Finned surfaces were designed to enhance heat transfer further if the cooling duct can be divided into many smaller ducts. Schematic of the fins used can be seen in Fig. 2. The waste heat that is going to be removed in this case is equal to the heat loss through the duct and surface as seen in Eq. 8:

$$Q_s + Q_D = \left(U_s + U_D\right) \left(T_{PV} - T_A\right) \tag{8}$$

where Q_D is the duct heat loss (W/m^2) and U_D is the duct cooling thermal resistance (W/m^{2}K).

2.1.2 Aerodynamics Drag

The pressure drop in one duct, if fins are used according to [15], can be calculated using Eq. 9,

$$\Delta P = f_D \frac{c}{d_H} \frac{\rho_A V_0^2}{2} \tag{9}$$

where f_D is the friction factor in the duct, c is the airfoil chord length, d_H is the hydraulic diameter, ρ_A is the air density and V_0 is the aircraft velocity.

The total drag force caused by ducts is given by the duct area multiplied by the pressure drop and the number of fins or ducts:

$$F_D = \Delta P A_{duct} N_{fins} \tag{10}$$

where A_{duct} is the cross-sectional area of the duct and N_{fins} is the total number of fins.

Once the aerodynamic drag is known, the power required to overcome the increase in drag force caused by the cooling duct can be calculated using Eq. 11:

$$P_{required} = F_D V_0. \tag{11}$$

The power gained (in W) by using a cooling duct as explained above can be calculated using Eq. 12:

$$P_{gain} = \Delta Q_{Loss,NoDuct} - \Delta Q_{Loss,WithDuct} \tag{12}$$

where ΔQ_{Loss}, the power loss in watts due to temperature difference with and without cooling duct, can be calculated using Eq. 13:

$$\Delta Q_{Loss} = \eta_{PV,L} Q_{PV} \left(T_{PV} - 298\right) \tag{13}$$

where $\eta_{PV,L}$ is the solar cell power coefficient and T_{PV} is the change in PV temperature over standard test conditions with conventional cooling and with the cooling duct.

2.2 Numerical Analysis

The analytical model described in the *Analytical* section above is limited to a flat plate and a rectangular duct since it was used initially to obtain an optimum duct height and did not represent the actual airfoil. Therefore, a CAD model of the Clark Y Airfoil, using Autodesk Inventor Professional, was created incorporating the optimised duct height of 2 mm provided by the MATLAB® model. ANSYS Fluent v14.5 was used to obtain the lift and drag characteristics of the baseline Clark Y and modified airfoil with the duct. ANSYS Fluent was also used to evaluate the heat transfer for the solar cells and obtain temperature changes between the baseline and modified models. The Clark Y airfoil coordinates were obtained from [16]. Both 2D and 3D models were used for the analysis. The 2D model was used to obtain lift and drag force coefficients, while the 3D model was used to obtain the temperature changes between the baseline and modified airfoils.

2.2.1 Preliminary Designs

Before arriving to the final modified design (denoted as Final design in Tab. 2 and Fig. 3) there were several preliminary CAD designs created to evaluate the best possible lift and drag coefficients achieved with a cooling duct. Designs 1, 2 and 3 featured a cooling duct with an outlet on the top of the wing and Design 4 had the duct outlet at the bottom just like the final design. The difference between the Design 4 and Final design is in the size of the duct, where the latter has a slightly larger duct. Figure 3 shows schematic of the four preliminary and final designs. The inlet position of the duct is the same for all of the designs considered.

Table 2 Lift and drag coefficients for the preliminary, baseline and modified airfoil designs.

Design	C_l	C_d	F_l (N)	F_d (N)	L/D	% δ in Lift	% δ in Drag
Baseline	0.316	0.0238	7.52	0.567	13.27	0	0
1	0.240	0.0289	5.71	0.686	8.32	-24	21
2	0.237	0.0297	5.64	0.706	7.99	-25	25
3	0.302	0.0249	7.19	0.593	12.13	-4	5
4	0.269	0.0567	6.41	1.349	4.75	-15	138
Final	0.343	0.0270	8.17	0.641	12.73	9	13

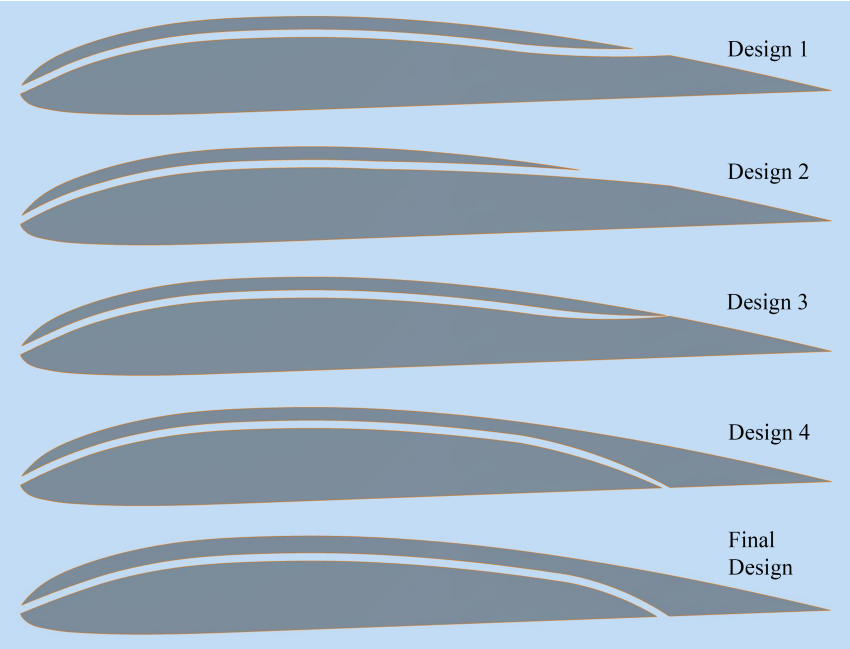

Figure 3: A schematic of the four preliminary and the final designs. Designs 1, 2 and 3 featured a cooling duct with an outlet on the top of the wing and Design 4 had the duct outlet at the bottom just like the final design.

After running computational fluid dynamics, the lift and drag coefficients were obtained for all the designs as shown in Table 2. Designs 1 and 2 which had the cooling duct outlet located on the top of the wing resulted in the airfoils generating lower lift and much higher drag than the baseline design. Design 3 was similar to Designs 1 and 2 but with the exception of smaller duct height at the outlet which resulted in the lowest drag and lift force generated compared to all designs. With reduced airflow through the duct, Design 3 would not be beneficial for efficiently reducing the solar cell temperatures. An alternate design for the cooling duct would be placing it at the bottom of the airfoil to evaluate the airfoil characteristics. Design 4 produced a very high increase in drag and low lift due to the narrow duct outlet. Hence the duct height was increased and the Final design was produced which

showed the best performance from all the designs. Therefore, the final design was selected since the airfoil generated more lift compared to the baseline and lower drag coefficients compared to the other designs.

2.2.2 2D Model Set-up

A flow domain was constructed for all 2D models which was 10 times the size of the airfoil chord length in the upstream and 20 times the sizer of the airfoil chord length in the downstream of the airfoil. This corresponds to a domain with a C-mesh of radius 2 m and length 4 m in order to capture the wake downstream of the trailing edge of the airfoil. These dimensions were selected after numerous tests which involved varying the domain size as shown in Fig. 4 and observing the effect of the lift and drag coefficients. The plot shows that the lift coefficient starts to converge after approximately $20\times$ chord length downstream and oscillates. By observing this trend it can be concluded that $20\times$ chord length is the optimum size for computational efficiency.

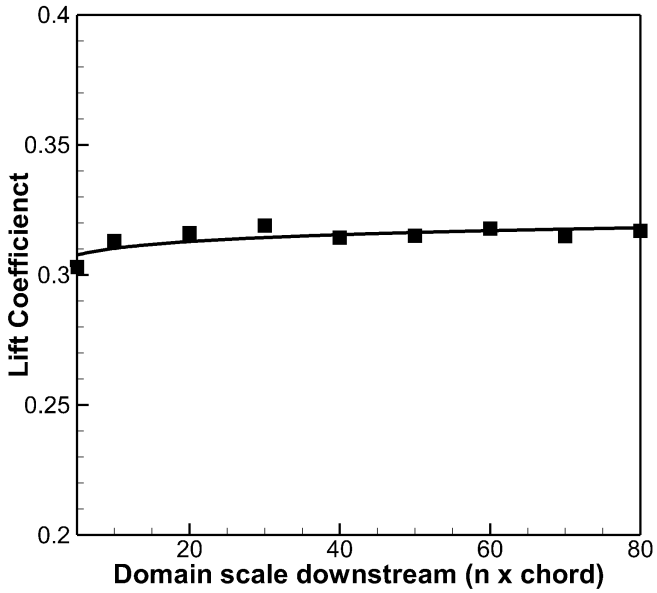

Figure 4: Variation of airfoil lift coefficient as a function of domain size downstream of the airfoil normalized with the airfoil chord length (c).

Figure 5 shows the domain size and a tetrahedral mesh which was selected for computational efficiency [17]. Sphere of influences with decreasing radius and element size was also employed in order to increase mesh density towards the airfoil. Edge Sizing around the airfoil geometry was selected to increase the number of elements so that the boundary layer can be captured more accurately. This can be seen in Fig. 7 which shows an enlarged view of the Baseline and Modified Airfoil Mesh. A y^+ of 4 was achieved to model the viscous sub-layer and improve the simulation accuracy. Figure 6 shows the outcome of 2D mesh resolution analysis for both final baseline and modified airfoils. As it can be seen from Fig. 6, the final baseline and modified airfoil models element numbers were selected to be 204,063 and 176,089 elements, respectively.

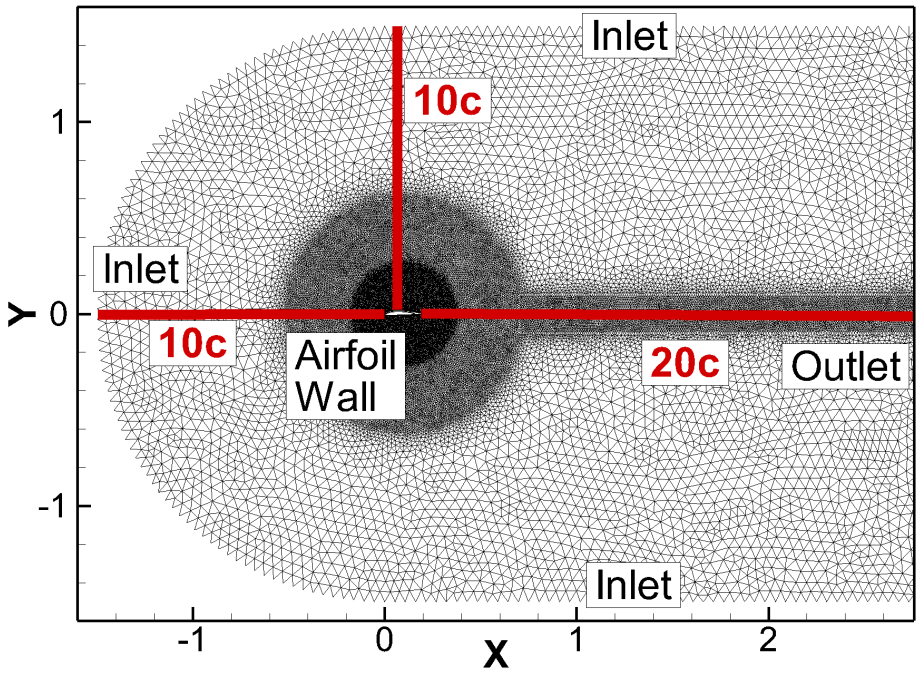

Figure 5: Sample of the C-Mesh type used for both models along with the domain size with respect to the size of the chord of the airfoil. Relevant boundary conditions are highlighted on the image. The Inlet represents "velocity-inlet" where the desired velocities were assigned. The Outlet was the "pressure-outlet" where the gauge pressure was set to zero and the wall was the selection of the airfoil surface. The X and Y axis unit is in meters.

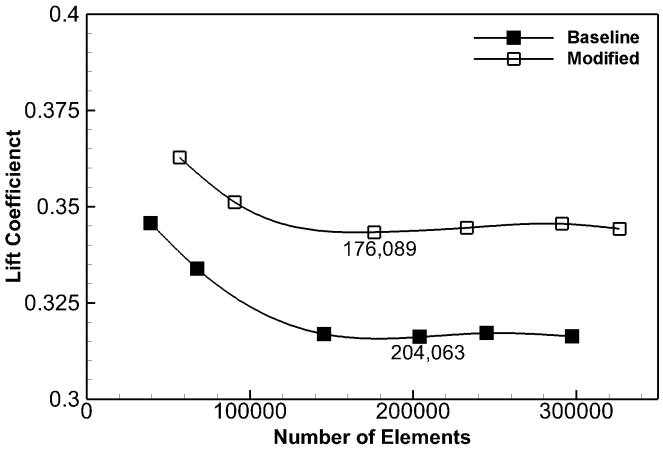

Figure 6: 2D Mesh resolution analysis for the final baseline and modified airfoils. Lift coefficient is used to determine the number of mesh.

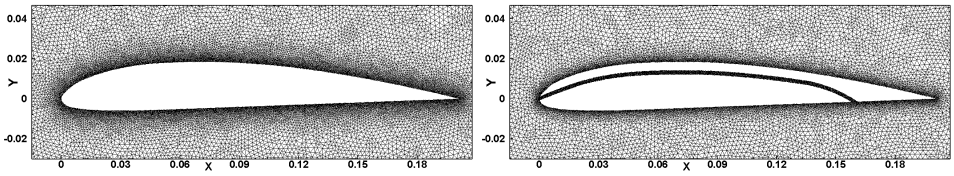

(a) Baseline Mesh (b) Modified Mesh

Figure 7: Enlarged View of (a) Baseline and (b) Modified Airfoil Mesh. The X and Y axis unit is in meters.

The same physical settings were applied for the baseline and modified 2D airfoil models. A standard $k - \epsilon$ model was used since the lift and drag coefficients obtained were close to the existing experimental data in the literature as reported in [18]. This turbulence model was selected since its accurate in predicting flows with boundary layer separation when combined with a fine mesh as was also suggested by previous studies [17]. In addition, it was important to analyse the airfoils for turbulence which can be more accurately solved with this model. Pressure based solver was used since the flow is incompressible. Both models utilised the same boundary conditions as depicted in Fig. 5. The Inlet represents "velocity-inlet" where the desired velocities were assigned. The Outlet was the "pressure-outlet" where the gauge pressure was set to zero and the wall was the selection of the airfoil surface. The spatial discretization for pressure, momentum, turbulent kinetic energy, and dissipation rate were selected to be second order. The gradient selected was least squares method and the scheme chosen was a coupled solver. These settings were used since it provided the best convergence. The chord length of 0.2 m was selected in the reference values in order to calculate the lift and drag coefficients. The convergence criterion levels were set to 1×10^{-5} since this was found to be sufficient for most applications and the same criteria was used for the 3D model.

Per unit length of lift and drag coefficients were calculated using Eq. 14:

$$C_L, C_D = \frac{F_L, F_D}{0.5\rho c V_0^2}. \tag{14}$$

Altitude variation was performed by changing the properties of air under the material section of ANSYS Fluent where the values were obtained from the MATLAB® code as discussed in the *Analytical* section.

2.2.3 3D Model Set-up

A flow domain was constructed which was 5 times size of the airfoil chord length. It is comprised of a rectangular mesh with a $1c$ depth and domain with a square of sides $1\ m$ (equivalent to $5c$). Figure 8 shows that the lift coefficient variation for various downstream domain sizes. It can be seen, similar to what was shown and discussed for the 2D Model case in section 2.2.2, the lift coefficient starts to converge after approximately $20\times$ chord length downstream and oscillates.

Figure 9 shows the domain size and a tetrahedral mesh which was selected for computational efficiency. Edge sizing around the airfoil geometry was selected to increase the number of elements so that the boundary layer can be captured more accurately. Figure 10 shows the outcome of 3D mesh resolution analysis for both final baseline and modified

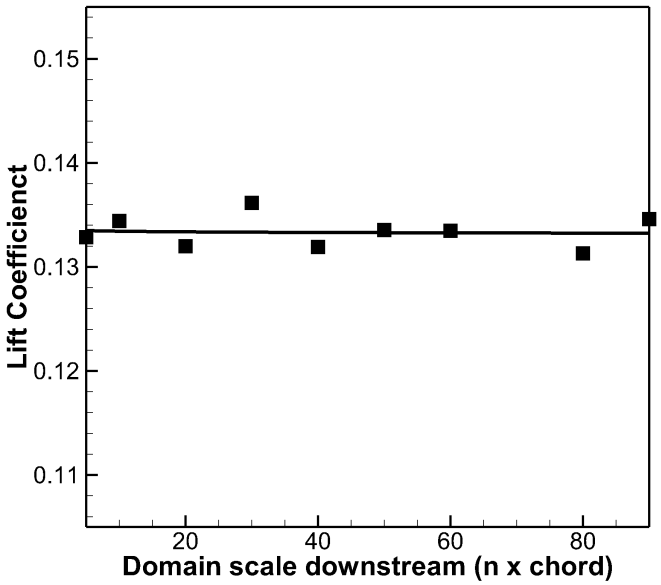

Figure 8: Variation of 3D wing lift coefficient as a function of domain size downstream of the wing model normalized with the wing's chord length (c). Solid line shows the best fit line to the data.

airfoils. A y^+ value between 30 and 50 was selected to model the log layer since mesh size was a consideration for the computational power available. As it can be seen from Fig. 10, the final baseline and modified airfoil models element numbers were selected to be 1,043,942 and 2,048,421 elements, respectively.

All the physical settings listed and explained in the *2D Model Set-up* were applied for the baseline and modified 3D airfoils as well. In addition, the following settings were also used for 3D models. The energy solver was used for heat transfer analysis and all parts under the boundary conditions were assigned coupled thermal conditions which allowed conduction and convection. The inlet and outlet temperatures in the boundary conditions were set to the same ambient air temperature. In the material setup, the properties of the solar cell, EVA, and ABS plastic were defined. Summary of the material properties are listed in Table 1. The solar cell was selected under cell zone conditions and one energy source was used.

The solar heat flux was 950 W/m^2 and using the cell efficiency of 22% (which has thickness of 200 microns) the waste heat is calculated as 741 W/m^2. Then the heat generation rate value was found to be 3.71 MW/m^3 as shown in Eq. 16.

$$\dot{E}_{gen,cell} = \frac{Q_H}{t_{PV}} \tag{15}$$

where $\dot{E}_{gen,cell}$ is the heat generation rate per volume from the PV cell (W/m^3) and t_{PV} is the thickness of the PV cell (m).

$$\dot{E}_{gen,cell} = \frac{741}{0.0002} = 3.71\ MW/m^3 \tag{16}$$

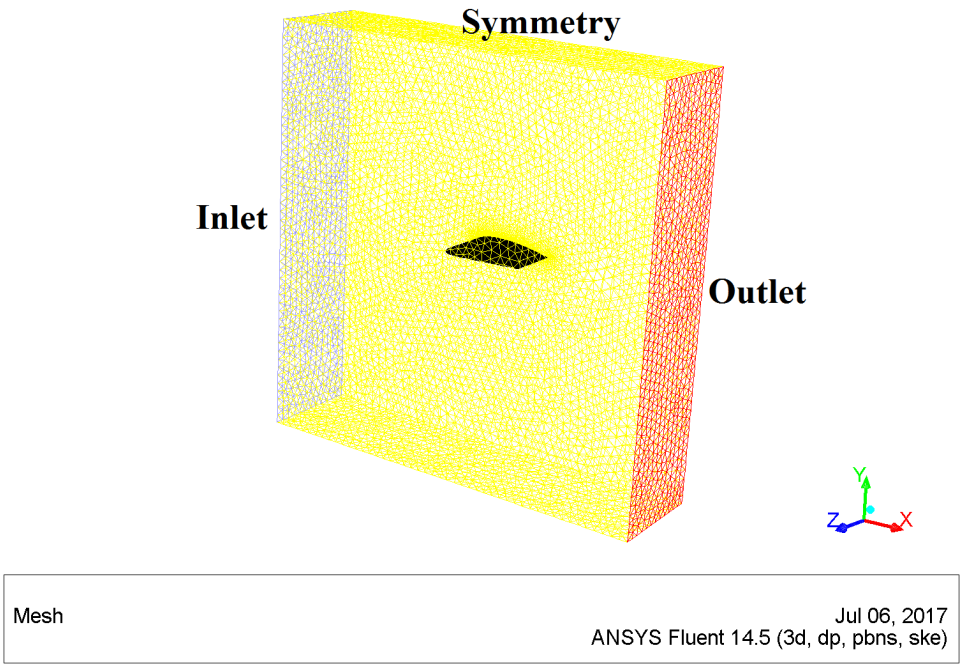

Figure 9: Schematic of the 3D domain with the relevant boundary conditions highlighted on the image. The black surface in the middle of the domain is the wing.

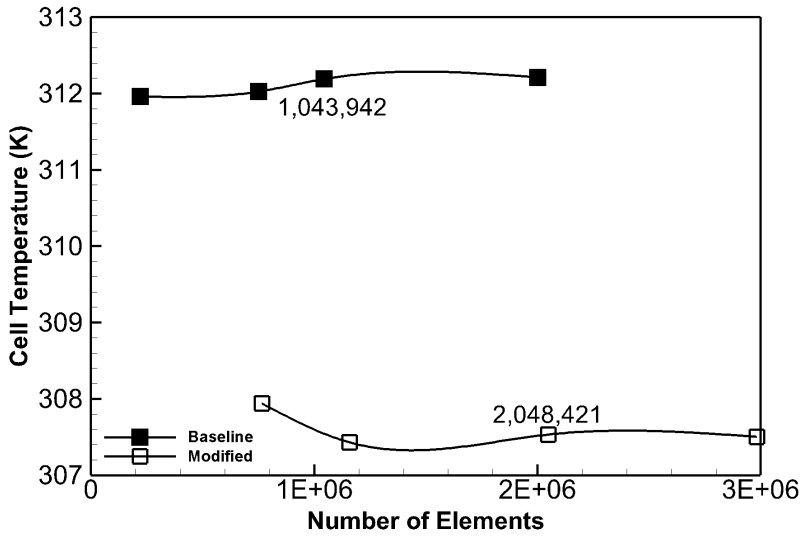

Figure 10: 3D Mesh resolution analysis for the final baseline and modified airfoils. Middle point on the PV cell temperature is used to determine the number of mesh.

Altitude variation was performed by changing the properties of air under the material section of ANSYS Fluent where the values were obtained from the MATLAB® code.

3 Results and discussions

The results of the two different analysis performed is described within this section. A detailed discussion and explanation of results are given along with sources of error.

3.1 Analytical solutions

For the analytical analysis, the aircraft was assumed to be flying at cruising conditions with a velocity of 15 m/s at an altitude of 1000 m above the sea level. The solar radiation was considered to be at a constant value of 950 W/m^2 and the air temperature at an altitude of 1000 m was 26.5°C. The MATLAB® model did not include finned heat sinks.

Figure 11 shows the difference between the electrical power gained by a reduction in solar cell temperature and the electrical power required to overcome the drag force caused by the cooling duct. By observing the trend in the graph, the overall change in power decreases with an increase in duct height. At a duct height of 4 mm, the cooling duct is rendered ineffective since the power gained by cooling is equal to the power loss by drag. Hence, an optimum value for duct height, $i.e.$ 2 mm can be considered in Fig. 11 for the cruising conditions mentioned earlier.

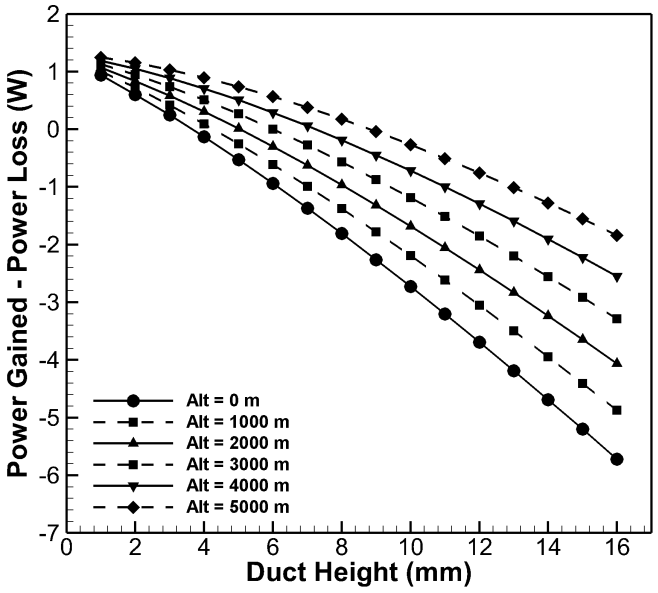

Figure 11: Change in Electrical Power Gain and Loss due to drag for various duct heights (with altitude).

Aircraft velocity significantly affects the solar cell temperature and this effect can be seen in Fig. 12 which shows that the solar array power is 66 W at 1 m/s without ducting. As

the aircraft velocity increases, the array power starts to increase with a higher gradient until 10 m/s where the gradient decreases and there is a gradual increase in array power. The reason for this trend is that the solar cell efficiency decreases with an increase in temperature, therefore resulting in lowered power outputs at lower velocities, due to decreased cooling. As the velocity of air increases, the convective heat transfer coefficient increases hence maximising heat transfer. The cooling duct has a significant effect in cooling at lower velocities and the average power gained at cruising conditions is around 2 W.

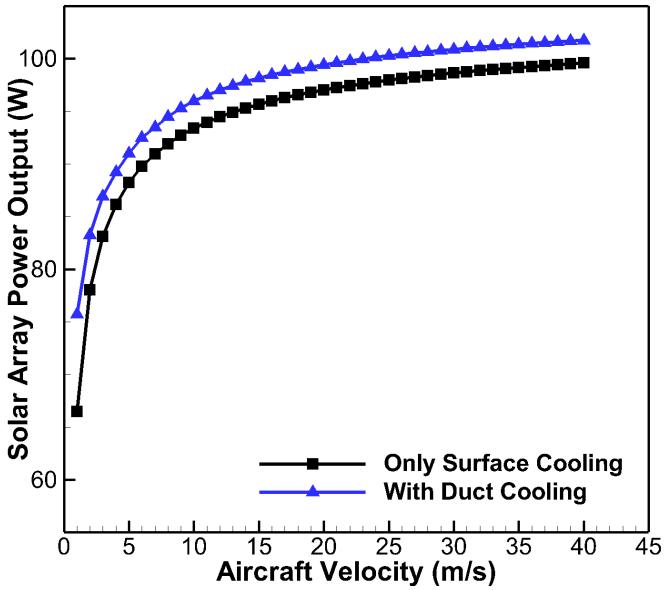

Figure 12: The solar array power output from the aircraft as a function of the aircraft velocity.

3.2 Numerical solutions

Since the MATLAB® model was limited to a flat plate and a straight rectangular duct, the actual changes in velocities and temperatures could not be modelled like the Clark Y airfoil. Hence, computational fluid dynamics (CFD) was performed at the exact same cruising conditions as previous section to determine the lift and drag coefficients of the modified airfoil.

All results presented and discussed in this section are from the analysis performed on the airfoil models when the aircraft was at cruising conditions. This was at a velocity of 15 m/s and altitude of 1 km. The angle of attack was kept constant at 0°. Figure 13 shows the gauge pressure contours around the baseline and the modified airfoil. It can be seen that the pressure is slightly higher at the bottom of modified airfoil compared to the baseline case. Hence, the net pressure at the bottom of the modified airfoil is greater. Since the pressure contours for both airfoils on the top are similar, the increased pressure at the bottom for the modified airfoil results in increased lift over the baseline model by 0.7 N per meter.

Figure 14 shows velocity contours for both baseline and modified airfoils. It can be seen that there is no significant difference in the velocity contours on the top of both airfoils.

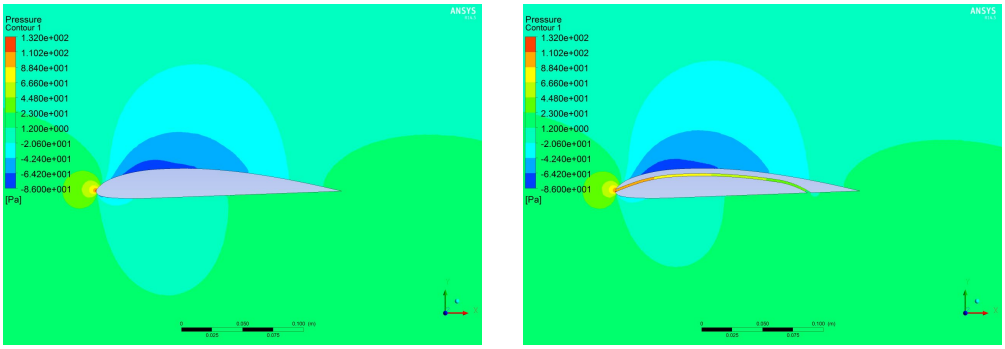

(a) Baseline (b) Modified

Figure 13: Gauge Pressure contours for both airfoils at a cruising velocity of 15 m/s, altitude of 1 km and zero angle of attack. The contour limits are the same for both graphs.

However, the velocity at the bottom of the modified airfoil is less compared to the baseline as indicated by the orange area. This is because the stagnation point at the duct inlet has changed and now part of the flow goes through the duct. It then results in a lower velocity at the bottom since the pressure has increased as shown in Fig. 13. The flow velocity inside the duct is approximately 6 m/s.

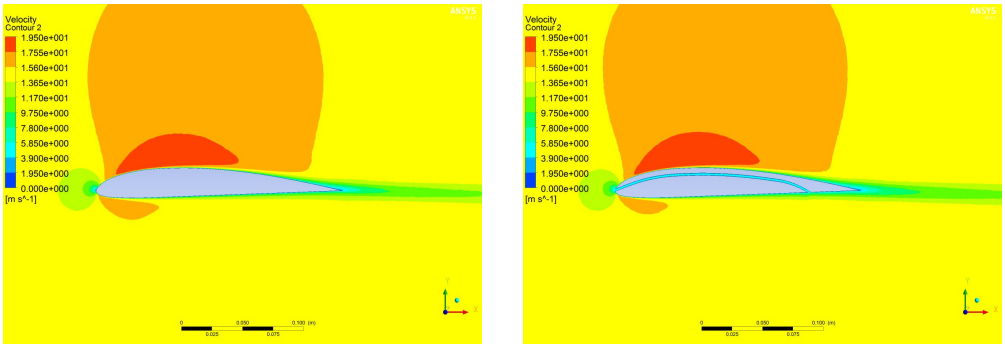

(a) Baseline (b) Modified

Figure 14: Velocity contours for both airfoils at a cruising velocity of 15 m/s, altitude of 1 km and zero angle of attack. The contour limits are the same for both graphs.

Figure 15 shows turbulent kinetic energy contour of the same conditions as of Figs. 13 and 14 around the baseline and modified airfoils. It is clearly seen that far-field flow has a very uniform and low distribution of turbulent kinetic energy. Once the approaching flow meets the leading edge of the airfoil all of the flow energy will be converted to stagnation energy. The red spot at the leading edge of the baseline airfoil as seen in Fig. 15a supports this. There is a maximum area of turbulent kinetic energy which can be seen doesn't exist as prominent as the modified case. This can be explained by the passage of the flow through the duct since the duct inlet is deliberately located at the leading edge stagnation point for the zero angle of attack case. The flow inside the duct will remain the same as that of free-

stream as shown by the uniform dark blue colour inside the duct. The other observation that can be made is the distribution of turbulent kinetic energy in the near-wake of the airfoil. The near-wake flow will be explained in more detail in Figs. 18 and Fig. 19.

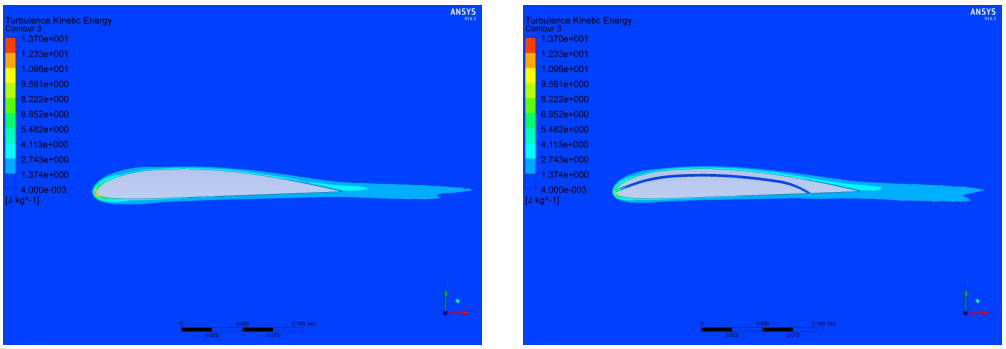

(a) Baseline (b) Modified

Figure 15: Turbulence Kinetic Energy contours for both airfoils at a cruising velocity of 15 m/s, altitude of 1 km and zero angle of attack. The contour limits are the same for both graphs.

Table 3 summarises the baseline and modified airfoils lift and drag distribution at cruising conditions. This shows that the modified airfoil's lift coefficient has increased by 9% while the drag coefficient has decreased by 13% per unit length over a 2.9 m span.

Table 3 Aerodynamic characteristics at cruising conditions.

Airfoil	C_l	C_d	Lift (N)	Drag (N)
Baseline	0.316	0.0238	7.5	0.56
Modified	0.343	0.027	8.2	0.64

Figure 16 shows the lift to drag ratio as a function of Reynolds number for the baseline and modified airfoils. It can be seen that the values are very close and the lift to drag ratios have a slight deviation. This indicates that the drag generated by the duct is compensated with an increase in lift. From the computational results, the lift to drag ratio between baseline and modified airfoils varies between 0.17 to 5.1 %.

The drag polar, as seen in Fig. 17, for the baseline and modified airfoil, shows that with an angle of attack over $\pm 5°$, the lift coefficient decreases considerably and the resulting drag coefficient increases. It shows that the performance of the modified airfoil is poor for those ranges of angles of attack. For the Clark Y airfoil, the optimum angle of attack lies between -5°$\leq\alpha\leq$5° as shown by the baseline airfoil on the same graph. Since the airfoil is cambered an angle of attack between -5°$\leq\alpha\leq$5° is recommended as the performance of the modified airfoil is relatively good.

The general trend of the graphs in Fig. 18 shows that the Y/C ratio exponentially decreases as the turbulent kinetic energy increases. It can be noted that the turbulent kinetic energy reaches zero when Y/C = 0.1 and this is because the distance is increased in the y–direction away from the airfoil where there is no wake. The maximum kinetic energy

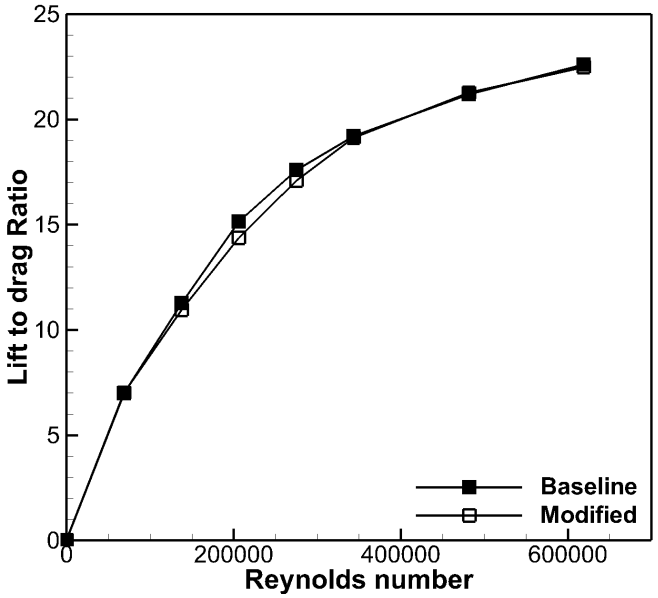

Figure 16: Lift to Drag Ratio vs. Reynolds Number for Baseline and Modified Airfoils.

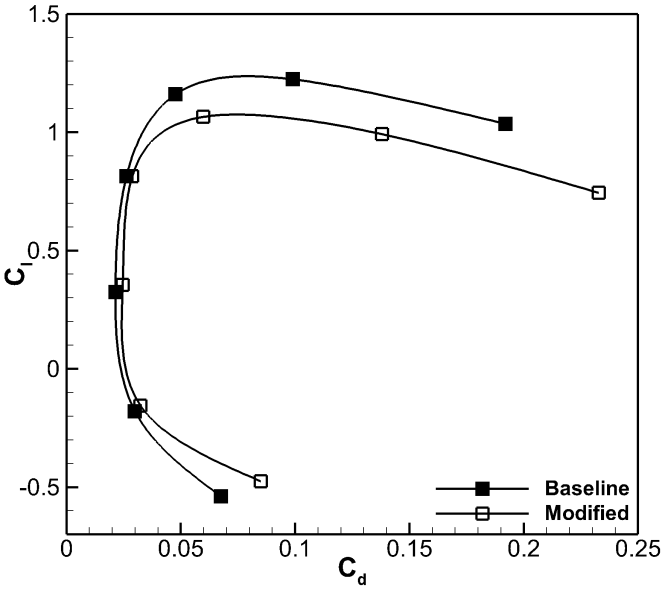

Figure 17: Drag Polar Graph for $Re = 206,000$.

was 3.2 m^2/s^2 as depicted by the triangle markers of the modified airfoil. For the baseline airfoil, this value was 2.8 m^2/s^2 and this shows that a higher turbulent kinetic energy results in increased drag which can be seen in Fig. 17. Another observation is that the maximum

turbulent kinetic energy occurs when Y/C = 0 and this is where the chord line of the airfoil passes through.

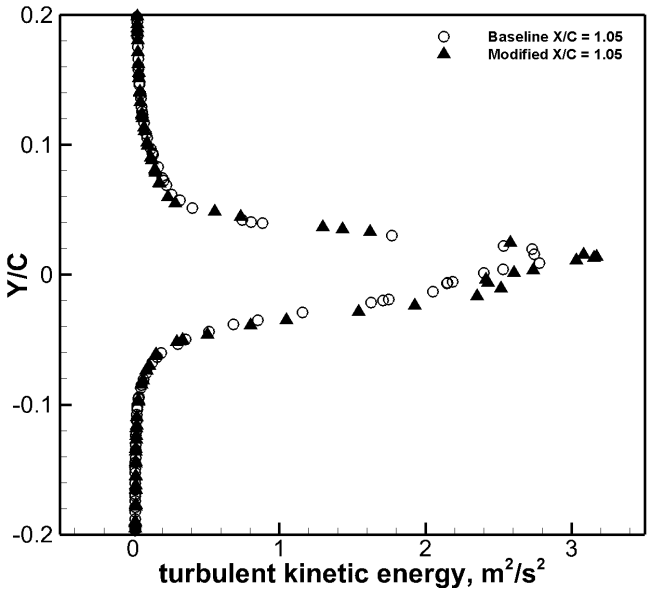

Figure 18: y–direction length over chord ratio against turbulent kinetic energy for the baseline and modified airfoils at a point 5% of the chord length from the trailing edge.

The graphs plotted in Fig. 19 show the strength of the turbulent kinetic energy for the baseline model as X/C ratio increases or when the measured points move away from the trailing edge. It can be observed that the maximum turbulent kinetic energy of 2.8 m^2/s^2 represented by the circle marker reduces to 0.7 m^2/s^2 as shown by the triangles when the X/C ratio increases. This explains that the turbulence is stronger at the trailing edge of the airfoil and then decreases as the energy is lost due to the circulation movements generated due to the pressure drag.

When observing all graphs in Fig. 20, the Y/C ratio exponentially increases with an increase in velocity until a maximum of 15 m/s. This is because the velocity value is measured away from the wake region where there is no disturbance in the flow and therefore it reaches the freestream velocity of 15 m/s. For X/C ratio increasing from 1.5 to 2, the Y/C ratio is greater when freestream velocity is reached. In addition, the lowest velocities of 13 and 11 m/s correspond to an X/C ratio of 1.5 and 2, respectively. This can be explained by the reduced turbulent energy as shown in Fig. 19 when moving away from the trailing edge and resultant increase in velocity at the end of the wake. For a fixed X/C ratio of 1.5, the lowest velocity is 11 m/s and 11.3 m/s for the modified and baseline airfoils, respectively. These results show that the modified airfoil has a larger wake since the velocity is slower compared to the baseline at the same point and a larger wake corresponds to an increased pressure induced drag.

The temperature distribution on the upper surface of the wing as shown in Fig. 21 is obtained when the aircraft is at cruising conditions where the altitude is 1 km and velocity is 15 m/s. The angle of attack of the wing is set to zero degrees. It can be clearly observed

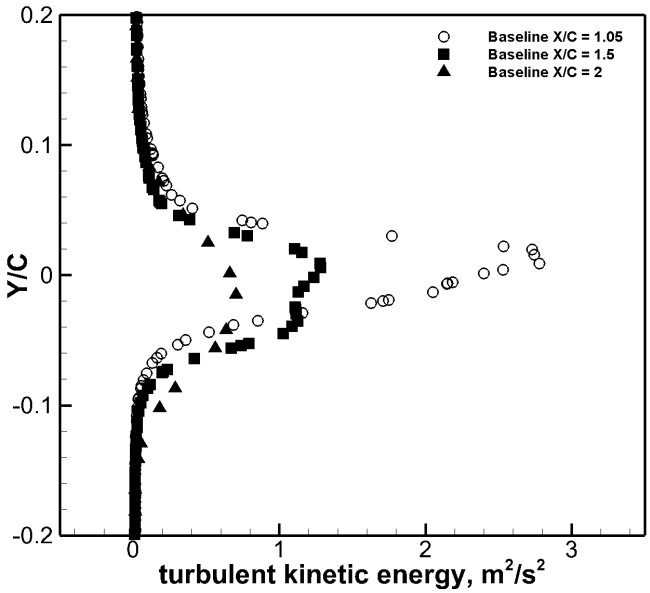

Figure 19: y–direction length over chord ratio against turbulent kinetic energy for the baseline airfoils at points 5, 50 and 100 % of the chord length from the trailing edge.

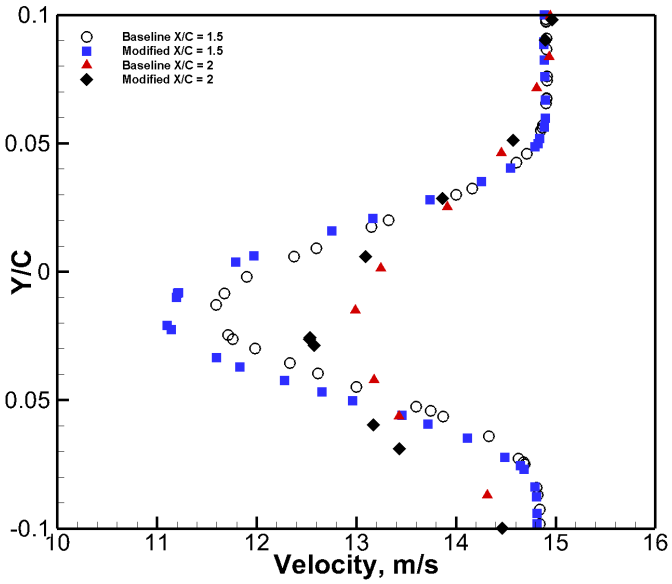

Figure 20: y–direction length over chord ratio against velocity for the baseline and modified airfoils at points 50 and 100 % of the chord length from the trailing edge.

that the modified airfoil has a lower surface temperature than the baseline airfoil as shown by the lighter colors over the wing surface which corresponds to lower temperatures.

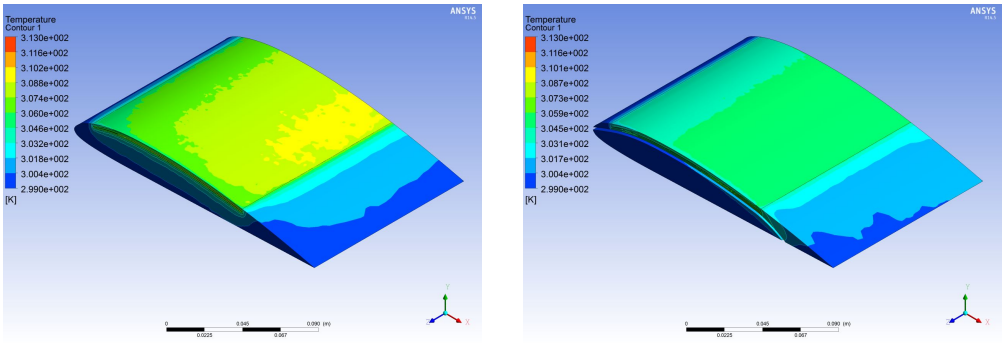

(a) Baseline (b) Modified

Figure 21: Temperature contours on the upper surface of the wing for both airfoils at a cruising velocity of 15 m/s, altitude of 1 km and zero angle of attack.

Figure 22a shows the change in solar cell temperature between the baseline and modified airfoil. At velocities below 4 m/s the cooling duct is completely ineffective. This is because the velocity in the duct is much slower than the aircraft velocity and therefore at lower speeds it tends to become stagnant. As a result, the temperature in the duct starts to increase slightly. As the velocity increases the solar cell temperature decreases exponentially and the maximum drop was found to be 3°C. This will increase the solar cell power by 0.5% per unit length of wingspan. The temperature difference between the modified and baseline airfoils starts to remain constant above velocities of 15 m/s. Figure 22b clearly identifies the relationship between altitude and solar cell temperature. As the altitude increases, the temperature drops but the temperature difference between the baseline and modified airfoils remains at around 3°C.

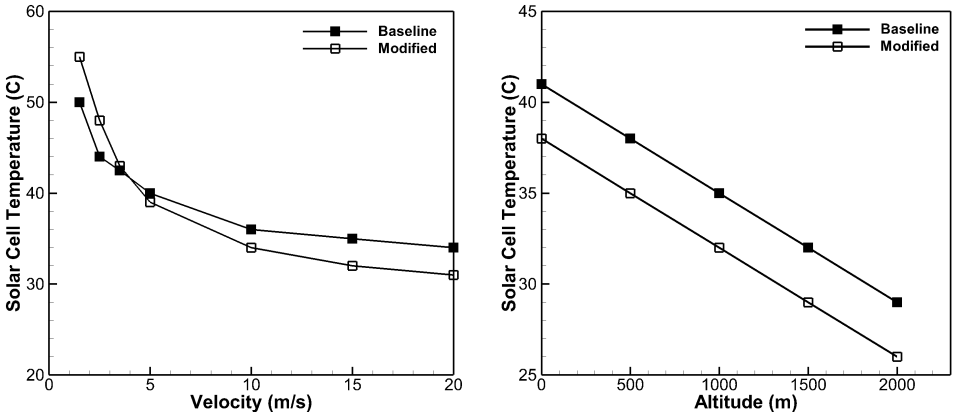

(a) altitude of 1000 m (b) velocity of 15 m/s

Figure 22: Distribution of the Solar cell temperature versus (a) aircraft velocity and (b) aircraft altitude with a solar heat flux of 950 W/m^2.

4 Conclusion

A concept was proposed which integrates a cooling duct inside the airfoil to provide convective cooling for the backside of solar cells. A MATLAB® program was first developed to model, size and provide optimum duct dimensions. Computational Fluid Dynamics (CFD) was also used to investigate the lift and drag characteristics of the modified airfoil. Heat transfer analysis on the solar array using CFD was performed to obtain solar cell temperatures of the baseline and modified design. The study investigated the lift and drag coefficients at different Reynolds numbers, angles of attack at cruising conditions and solar cell temperatures at different altitudes. From the analysis carried out on the cooling ducts, it is concluded that the design concept is beneficial to reducing solar cell temperatures. The maximum temperature drop by using the duct was found to be 3°C and this would increase the solar cell power by 0.5% per unit length of wingspan. This can be improved by optimising a finned heatsink design and using materials with higher thermal conductivity. CFD analysis on the baseline and modified airfoils showed that the cooling duct increased the lift force generated and was able to compensate for the increased aerodynamic drag. The wake results also showed that the modified airfoil has a larger wake since the velocity is slower compared to the baseline at the same location as the baseline airfoil, where the larger wake corresponds to an increased pressure induced drag.

References

[1] Patricia Mora Segado, Jesús Carretero, and Mariano Sidrach-de Cardona. Models to predict the operating temperature of different photovoltaic modules in outdoor conditions. *Progress in Photovoltaics: Research and Applications*, 23(10):1267–1282, 2015.

[2] Dubai Airport. Dubai meteorological office, 2009.

[3] M. D. Islam, I. Kubo, M. Ohadi, and A. A. Alili. Measurement of solar energy radiation in Abu Dhabi, UAE. *Applied Energy*, 86(4):511–515, 2009.

[4] Stuart J. McColl, Peter Rodgers, and Valerie Eveloy. Thermal management of solar photovoltaics modules for enhanced power generation. *Renewable Energy*, 82:14–20, 2015.

[5] Anthony J Colozza and James Dolce. Convective Array Cooling for a Solar Powered Aircraft. Final Contractor Report NASA/CR-2003-212084, National Aeronautics and Space Administration, 2003.

[6] R.E. Murzello, M. Nazarinia, and A. Hughes. Design of a cooling duct for solar cells on a solar powered unmanned aerial vehicle to improve performance. In *34th AIAA Applied Aerodynamics Conference*, 2016.

[7] Abe Silverstein. Scale effect on Clark Y airfoil characteristics from NACA full-scale wind-tunnel tests. Technical Report No. 502, National Advisory Committee for Aeronautics, 1935.

[8] SunPower. C60 Solar Cell Mono Crystalline Silicon, 2010.

[9] M. M. Rahman, M. Hasanuzzaman, and N. A. Rahim. Effects of various parameters on PV-module power and efficiency. *Energy Conversion and Management*, 103:348–358, 2015.

[10] John D. Anderson. *Introduction to flight*. McGraw-Hill, 8th edition, 2016.

[11] US Standard Atmosphere. Washington, DC: National oceanic and atmospheric administration. *National Aeronautics and Space Administration, and the United States Air Force*, 1976.

[12] Egbert Torenbeek. *Advanced Aircraft Design*. Wiley, 2013.

[13] F. Incropera. *Principles of heat and mass transfer*. John Wiley & Sons Singapore Pte. Ltd, 2013.

[14] Farivar Fazelpour, Majid Vafaeipour, Omid Rahbari, and Reza Shirmohammadi. Considerable parameters of using PV cells for solar-powered aircrafts. *Renewable and Sustainable Energy Reviews*, 22:81–91, 2013.

[15] Y. Cengel. *Introduction to thermodynamics and heat transfer*. McGraw-Hill, New York, 2nd ed. edition, 2008.

[16] Theodore Theodorsen. Theory of wing sections of arbitrary shape. Technical Report NACAâŁ"1932-411, National Advisory Committee for Aeronautics, 1932.

[17] Ran Duan, Wei Liu, Luyi Xu, Yan Huang, Xiong Shen, Chao-Hsin Lin, Junjie Liu, Qingyan Chen, and Balasubramanyam Sasanapuri. Mesh type and number for the CFD simulations of air distribution in an aircraft cabin. *Numerical Heat Transfer, Part B: Fundamentals*, 67(6):489–506, 2015.

[18] Charles H. Zimmerman. Characteristics of Clark Y airfoils of small aspect ratios. Technical Report NACA-1933-431, National Advisory Committee for Aeronautics, Jan 1933.